

# Origin of a shallow electron pocket: $\beta$ -band in $\text{Co}_{1/3}\text{TaS}_2$ studied by angle-resolved photoemission spectroscopy

Wojciech Sas,<sup>1,2</sup> Yuki Utsumi Boucher,<sup>1</sup> Seyed Ashkan Moghadam Ziabari,<sup>1</sup> Gaurav Pransu,<sup>1</sup> Trpimir Ivšić,<sup>3</sup> László Forró,<sup>4</sup> Ivana Voborník,<sup>5</sup> Jun Fujii,<sup>5</sup> Naveen Singh Dhami,<sup>1,\*</sup> Bruno Gudac,<sup>6</sup> Mario Novak,<sup>6</sup> Neven Barišić,<sup>6,†</sup> Ivo Batistić,<sup>6,†</sup> and Petar Popčević<sup>1,‡</sup>

<sup>1</sup>*Institute of Physics, 10000 Zagreb, Croatia*

<sup>2</sup>*Institute of Nuclear Physics Polish Academy of Sciences, 31-342 Kraków, Poland*

<sup>3</sup>*Ruder Bošković Institute, 10000 Zagreb, Croatia*

<sup>4</sup>*Department of Physics and Astronomy, University of Notre Dame, Notre Dame, IN 46556, USA*

<sup>5</sup>*Istituto Officina dei Materiali (IOM)-CNR Laboratorio TASC, I-34149 Trieste, Italy*

<sup>6</sup>*Department of Physics, Faculty of Science, University of Zagreb, 10000 Zagreb, Croatia*

<sup>7</sup>*Institute of Solid State Physics, TU Wien, 1040 Vienna, Austria*

We investigated the electronic structure of Co-intercalated 2H-TaS<sub>2</sub> using angle-resolved photoemission spectroscopy (ARPES). In the compound Co<sub>1/3</sub>TaS<sub>2</sub>, the main electronic bands closely resemble those of pristine 2H-TaS<sub>2</sub>, with no clear signs of band folding. However, a shallow electron pocket, referred to as the  $\beta$ -feature, was detected at the Fermi level near the corner of the superlattice Brillouin zone. The surface vs bulk origin of this feature is debated, as it cannot be reproduced using standard DFT calculations. To resolve this, we employed cluster perturbation theory (CPT) to incorporating an exact treatment of strong electron correlations (U) on the cobalt sites, going beyond DFT+U approximation. To further substantiate this, we studied an underdoped sample, Co<sub>0.22</sub>TaS<sub>2</sub>, where a reduced charge transfer leads to different Co orbital character near the Fermi level. We find that its electronic structure closely resembles that of undoped 2H-TaS<sub>2</sub>, and crucially, lacks the  $\beta$ -feature. Our results demonstrate that the  $\beta$ -feature is of the bulk origin emerging from the strong electronic correlations where both the Co charge state and long-range crystallographic order play an important role. This work highlights the need for accurate treatment of electron correlations when studying intercalated transition metal dichalcogenides.

## I. INTRODUCTION

Two dimensional magnetic materials are gaining attention because of their potential for spintronic applications and engineering of magnetic heterostructure devices [1]. Among them, transition metal dichalcogenides (TMDs) intercalated by magnetic atoms are extensively being reinvestigated after half a century from their discovery [2, 3]. Their structural diversity, complex and rich electronic and magnetic properties offer a versatile playground to explore intricate interplay among symmetry, magnetic interactions, and electron correlations, that can also be controlled by external fields [3–6]. Systems intercalated with cobalt attract special attention, mainly due to the large anomalous Hall effect observed in 2H-NbS<sub>2</sub> and 2H-TaS<sub>2</sub> intercalated compounds [7–15]. In this paper, we focus on Co<sub>1/3</sub>TaS<sub>2</sub>, which features a hexagonal lattice with space group  $P6_322$ . Intercalated Co atoms occupy octahedral site coordinated by S atoms from layers above and below, and form  $\sqrt{3} \times \sqrt{3}$  superlattice rotated by 30° from the 1×1 unit cell of the parent compound 2H-TaS<sub>2</sub> [16–19]. It is long known that Co<sub>1/3</sub>TaS<sub>2</sub> (also denoted as CoTa<sub>3</sub>S<sub>6</sub>) exhibits antiferromagnetic (AF) ordering below  $T_N = 35$  K [17, 18], though details of its magnetic structure remained elusive [19].

Recently, new progress in the field was achieved when a systematic investigation by Park *et al.* [20], revealed two dis-

tinct magnetic phases in Co<sub>x</sub>TaS<sub>2</sub> around  $x \sim 1/3$ . In the overdoped regime ( $x \geq 0.330$ ) the system hosts AF phase below 35 K, with the magnetic structure found to be coplanar helical order [20]. In contrast, the underdoped regime ( $0.299 \leq x \leq 0.325$ ) hosts two distinct AF phases, the first one setting in at  $T_{N1} \approx 38$  K, and second one at  $T_{N2} \approx 26.5$  K accompanied by a large anomalous Hall effect (AHE). Although a small ferromagnetic component is observed below  $T_{N2}$ , such weak ferromagnetic moment is considered insufficient to explain the observed large anomalous Hall coefficient [14]. The magnetic structure below  $T_{N2}$  has been uncovered to be a tetrahedral triple- $\mathbf{q}$  magnetic ordering by neutron diffraction experiments [15, 21]. This state arises from the superposition of three coplanar 120° antiferromagnetic modulations, resulting in a non-coplanar spin texture that generates the finite Berry curvature characterized by a net scalar spin chirality and can lead to a spontaneous topological Hall effect (THE).

The substantial changes observed in physical properties of Co<sub>x</sub>TaS<sub>2</sub> with  $x \leq 0.325$  compared to  $x \geq 0.330$  cannot be explained by a simple shift of the Fermi level with increasing cobalt concentration. If these differences were purely electronic in origin, they would require a drastic reconstruction of the band structure and Fermi surface topology. Indeed, significant departures from rigid band shift have already been observed in related intercalated compounds such as Co<sub>1/3</sub>NbS<sub>2</sub>, Cr<sub>1/3</sub>NbS<sub>2</sub>, and Ni<sub>1/3</sub>NbS<sub>2</sub>, where angle-resolved photoemission spectroscopy (ARPES) revealed a distinct shallow band near the Fermi level, commonly referred to as the  $\beta$  band, likely originating from intercalant Co/Ni orbitals [10–12, 22, 23]. These findings underscore the critical role of intercalant-derived electronic states in shaping the low-energy

\* Current affiliation: Université Paris-Saclay, CNRS, Laboratoire de Physique des Solides, 91405 Orsay, France

† ivo@phys.hr

‡ ppopcevic@ifs.hr

electronic structure and their potential impact on topological transport phenomena. In addition to these electronic effects, the observed sensitivity of the magnetic ground state to the Co concentration may also reflect competing magnetic interactions. Notably, the 1/3 intercalation level gives rise to a highly frustrated magnetic environment, where subtle imbalances can tip the system toward different magnetic orders. Slight deviations from this concentration, either by under- or over-doping, appear to lift the frustration and favor one of the competing interactions, leading to qualitatively different magnetic and consequently transport properties.

In this study, we perform ARPES measurements on  $\text{Co}_{1/3}\text{TaS}_2$  and underdoped  $\text{Co}_{0.22}\text{TaS}_2$  to explore how variations in cobalt concentration influence the band dispersion and Fermi surface topology. To complement the experimental data, we also employ theoretical modeling that goes beyond conventional density functional theory (DFT). Specifically, we use cluster perturbation theory (CPT) to account for strong electronic correlations and the role of intercalant-derived states. This extended approach allows us to analyze the origin of the shallow electron band in  $\text{Co}_{1/3}\text{TaS}_2$ , commonly referred to as the  $\beta$  band, and draw conclusions applicable more generally to magnetically intercalated TMDs.

## II. EXPERIMENT AND METHODS

Single crystals of  $\text{Co}_{1/3}\text{TaS}_2$  were grown by chemical vapor transport method using iodine as the transport agent [2]. The grown single crystals were characterized by electrical resistivity measurement, X-ray diffraction, energy dispersive X-ray spectroscopy (EDX) and magnetic susceptibility. The EDX analysis indicated 32% intercalation. To achieve this level of intercalation, it was important to put  $\sim 15\%$  more Co than stoichiometric composition would indicate. Further in text this sample is referred to as  $\text{Co}_{1/3}\text{TaS}_2$ . Magnetic susceptibility revealed antiferromagnetic transition temperature at  $T_N = 37\text{ K}$ .  $T_{N2}$  was not observed in our crystal. The sample does show zero field magnetization below  $T_N$  (see Supplemental material) similarly as the double transition samples do below  $T_{N2}$  [14, 15, 21], although the values in our crystals are order of magnitude lower, and anomalous Hall effect is absent. Indeed, contrary to our EDX results, magnetic and transport properties (see Supplemental material) point to slight over doping according to Park *et al.* [20]. Temperature dependent electrical resistivity shows a kink at the magnetic transition temperature. Residual resistivity ratio (ratio of the room temperature resistivity to resistivity at 2 K) in our crystals was around 2.2 which is slightly higher than the one reported in double transition samples [14] indicating high sample quality. Analysis of X-ray diffraction data shows that the compound crystallizes in the hexagonal space group No. 182 ( $P6_322$ ), with lattice constants  $a = 5.76\text{ \AA}$  and  $c = 11.99\text{ \AA}$ . We have also synthesized a single crystal with 22% Co, as indicated by EDX. For it the starting material contained 33% of Co per Ta. The electrical resistivity exhibited a nonmetallic trend, varying only weakly with temperature. Magnetic susceptibility reveals ferromagnetic like transition around 25 K. The same behavior of 22%

intercalate was reported by Liu *et al.* [13].

Angle-resolved photoemission spectroscopy (ARPES) measurements were performed at the APE-LE beamline [24] of the Elettra synchrotron. The crystals were oriented along the high-symmetry  $\overline{\Gamma}\text{M}_0$  direction using Laue diffraction and then mounted on copper plates with silver epoxy. Clean surfaces were prepared by cleaving inside the ARPES main chamber under ultra-high vacuum (base pressure of  $3 \times 10^{-10}\text{ mbar}$ ) at 20 K. The incident photon energy ( $h\nu$ ) was varied between 30 and 90 eV. Most measurements were carried out at 20 K, below the magnetic ordering temperature of  $\text{Co}_{1/3}\text{TaS}_2$ . To compare the spectra below and above the magnetic transition, additional scans along the  $\overline{\Gamma}\text{M}_0$  direction and Fermi surface maps were recorded at 50 K. The photon beam was linearly polarized in the plane of the storage ring and oriented perpendicular to the analyzer slit. Photoelectrons were collected using a hemispherical DA30 analyzer equipped with a multi-channel plate and CCD detector. The overall energy resolution was approximately 30 meV.

The electronic band structure of  $\text{Co}_{1/3}\text{TaS}_2$  was calculated using Density Functional Theory (DFT) as implemented in the Quantum ESPRESSO package [25, 26]. We used a kinetic energy cut-off of 120 Ry for the plane-wave basis set and 1000 Ry for the charge density and potentials. To account for electronic correlations on the cobalt ions, we employed the DFT+U method following the approach of Dudarev *et al.* [27]. The on-site Hubbard interaction parameter,  $U = 5.77\text{ eV}$ , was computed using a linear-response formulation of constrained DFT (LR-cDFT), implemented within the framework of density-functional perturbation theory (DFPT) [28–30]. The Brillouin zone was sampled using a  $10 \times 10 \times 5$   $k$ -point mesh without shift. The sharp cutoff of electron occupation at Fermi energy is modeled by a smearing technique proposed by Marzari and Vanderbilt [31], with a broadening width of 0.01 Ry.

Electronic correlations were investigated using Cluster Perturbation Theory (CPT) based on a Wannier-function representation of the spin-polarized DFT+U band structure. The calculations were performed within an energy window of  $\pm 1\text{ eV}$  around the Fermi level. Each cluster consisted of four Wannier nodes representing three Ta and one Co orbitals: the Ta-derived Wannier functions are centered in the triangular plaquettes between Ta atoms, whereas the Co Wannier functions are atom-centered. Local electron interactions on the Co orbitals were included via a Hubbard  $U$  term, with double counting corrected by adjusting the on-site energies. The many-body cluster Hamiltonian was solved exactly, while inter-cluster hoppings were treated perturbatively to construct the full CPT Green's function. The resulting spectral functions were unfolded to the extended Brillouin zone for direct comparison with ARPES measurements.

## III. RESULTS AND DISCUSSIONS

Fig. 1 shows the ARPES intensity plots of  $\text{Co}_{1/3}\text{TaS}_2$  measured at 20 K with photon energy  $h\nu = 72\text{ eV}$ . Panel (a) presents spectra collected along the  $\overline{\Gamma}\text{M}_0$  direction, where  $\text{M}_0$

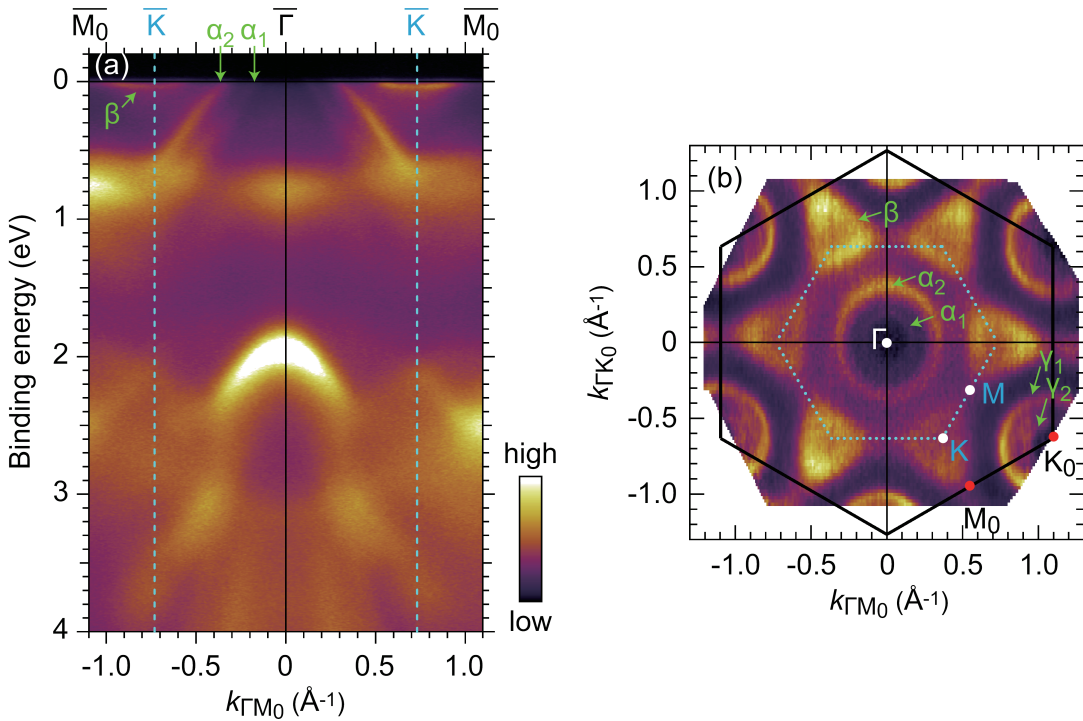


FIG. 1. (Color online) (a) ARPES intensity plot of  $\text{Co}_{1/3}\text{TaS}_2$  along  $\overline{\Gamma}\text{M}_0$  direction at 20 K measured with  $h\nu = 72$  eV. The vertical-dashed lines represent the boundaries of  $\text{Co}_{1/3}\text{TaS}_2$  surface Brillouin zone. (b) The Fermi surface map at 20 K with  $h\nu = 72$  eV. The black hexagon and the smaller blue hexagon shown in the dashed line represent the first Brillouin zone of 2H-TaS<sub>2</sub> and  $\text{Co}_{1/3}\text{TaS}_2$ , respectively.

corresponds to the high-symmetry point in the surface Brillouin zone (BZ) of the host 2H-TaS<sub>2</sub>, while  $\overline{\text{K}}$  marks the high-symmetry point of the  $\text{Co}_{1/3}\text{TaS}_2$  superlattice BZ. The main band features resemble those of pristine 2H-TaS<sub>2</sub> [32], with no evident band folding or splitting at the boundaries of the  $\text{Co}_{1/3}\text{TaS}_2$  BZ. Beyond an overall band shift due to charge transfer, slight redistribution of Ta and S atoms upon Co intercalation introduces a modulation into the host lattice. This modulation coupled with some occupational disorder of intercalated Co atoms, results in the observed broadening of the ARPES features compared to the parent compound.

Fig. 1(b) shows the corresponding Fermi surface map. The large black dashed hexagon and the smaller blue dashed hexagon indicate the surface Brillouin zones of 2H-TaS<sub>2</sub> and  $\text{Co}_{1/3}\text{TaS}_2$ , respectively. As in 2H-TaS<sub>2</sub>, double walled, cylindrical Fermi surfaces are observed around the  $\overline{\Gamma}$  point ( $\alpha_1$  and  $\alpha_2$ ) and the  $\overline{\text{K}}$  point ( $\gamma_1$  and  $\gamma_2$ ) [33, 34]. Compared to the parent compound, in  $\text{Co}_{1/3}\text{TaS}_2$ , the splitting between these double walls is more pronounced around the  $\overline{\Gamma}$  point due to band shifting, and more importantly, Co mediated interlayer hybridization. The same effect was also observed in  $\text{Co}_{1/3}\text{NbS}_2$  [10]. The inner FS ( $\alpha_1$ ) is very faint representing a bonding band. Additionally, a notable difference introduced by intercalation is the emergence of a triangular Fermi surface pocket, commonly referred to as the "β-feature", centered at the  $\overline{\text{K}}$  point. The band responsible for this Fermi surface pocket is a shallow electron like band around the  $\overline{\text{K}}$  point which is marked by the blue dashed line in Fig. 1(a). Simi-

lar features have been reported in other intercalated dichalcogenides such as  $\text{Co}_{1/3}\text{NbS}_2$  [10–12],  $\text{Ni}_{1/3}\text{NbS}_2$  [23], and  $\text{Cr}_{1/3}\text{NbS}_2$  [22, 35].

To study the possible effect of magnetic ordering on the band structure, we also measured the ARPES spectra and the Fermi surface above the magnetic transition ( $T_N = 37$  K) at 50 K. There was no noticeable difference between the spectra at 20 K and 50 K (see Supplemental material). The presence of the β-feature above and below  $T_N$  confirms that the origin of the shallow electron pocket is unrelated to the magnetic transition. The antiferromagnetic TMD series of  $\text{Co}_{1/3}\text{NbS}_2$  and  $\text{Ni}_{1/3}\text{NbS}_2$  also did not exhibit any electronic structure changes across magnetic transitions [23, 36].

Although the β-feature has been experimentally observed among other transition-metal-intercalated TMDs, its origin remains debated. One possible explanation, as a surface state, has been proposed mainly based on the fact that in  $\text{Co}_{1/3}\text{NbS}_2$  its relative intensity depended on the surface termination or position [11]. However, its variation with excitation photon energy and its observation in soft X-ray ARPES [12] do not convincingly support this interpretation. Furthermore, our DFT calculations considering a slab with two layers of  $\text{Co}_{1/3}\text{TaS}_2$  do not support the surface-effects origin of the β-feature (see Supplemental material).

Apart from the β-feature, the DFT calculations successfully reproduce the experimentally observed band structures of  $\text{Co}_{1/3}\text{NbS}_2$  [36] and  $\text{Ni}_{1/3}\text{NbS}_2$  [23]. In particular, the DFT bands unfolded into the large parent-compound BZ match the main band features observed by ARPES. The same is true for

$\text{Co}_{1/3}\text{TaS}_2$  (See Appendix B).

We attribute the origin of the  $\beta$ -feature to strong correlation effects that cannot be captured by standard DFT+U. In our earlier study of  $\text{Co}_{1/3}\text{NbS}_2$  [36], the feature was addressed within a slave-boson approach where it was shown that strong local Coulomb interactions on the Co sites lead to a renormalization of the Co-host hybridization and a shift of the Co-derived states toward the Fermi level, resulting in the emergence of a narrow, resonance-like, band near the  $\bar{K}$  point, consistent with the experimentally observed  $\beta$ -feature. The strong correlation origin of this feature was also previously examined within the dynamical mean-field theory (DMFT) framework [37], yielding partial agreement with experiment. While those analyses provided qualitative evidence for the correlation-driven origin of the  $\beta$ -feature, in the present work, we adopt a more exact treatment of electronic correlations by employing cluster perturbation theory (CPT), initially proposed by Gros *et al.* [38] and further developed by Sénéchal *et al.* [39, 40]. In CPT, the Hubbard interaction is treated exactly at the cluster level, going beyond the mean-field approximation inherent to DFT+U, and capturing momentum-resolved spectral features that are not fully captured by DMFT.

Our CPT calculation is based on a Wannier function description of the band structure obtained from DFT+U for the spin-polarized system. We focus on the energy range around the Fermi level where the " $\beta$ -feature" occurs, in particular, from 1.0 eV below to 1.5 eV above the Fermi level. In this energy range, seven DFT bands can be accurately fitted (lower graph in Fig. 5) with a tight-binding type Hamiltonian obtained from the Wannier90 package [41] using seven Wannier functions. Several of the most dominant terms of the Wannier Hamiltonian are listed in Table I. While both spin channels share the same band structure, the Wannier representation of DFT results is spin-dependent. The six Wannier functions (spin-independent) are predominantly of Ta  $d$ -state character and are located in the space forming a triangle between three Ta atoms, not directly at the Ta atom positions (see Fig. 2(a)). The seventh Wannier function is spin-dependent: for electrons with spin up, its location is at the Co atom with spin down, and vice versa. This Wannier function primarily describes the unoccupied band above the Fermi level, while the Ta-derived Wannier functions capture the dispersions of the six bands crossing the Fermi level.

The CPT calculation requires a unified Hamiltonian that incorporates both spin projections. This is achieved by merging the Wannier Hamiltonians for the two spins, resulting in a Hamiltonian with eight Wannier functions per spin and per unit cell (shown in Fig. 2(a)). Two of these Wannier functions are located on Co atoms. To account for electron correlations, it is necessary to include the Hubbard interaction on the Co sites into the full CPT Hamiltonian. However, the single-particle part of the full Hamiltonian, obtained from DFT+U, already incorporates a mean-field approximation of the Hubbard interaction, and we must correct for double counting.

Double counting is a well-known and subtle problem that appears in all theories based on Wannier Hamiltonians going beyond a simple mean-field approximation, e.g., DMFT. It is extensively studied in many works [42–50]. Here, we adopt

the simplest approach, which is exact only in the localized limit: the double counting is corrected by modifying the Wannier on-site energies of sites with Hubbard interaction. Assuming the Hubbard interaction is given by:

$$H_{\text{Hub}} = U \cdot (n_{\uparrow} - 0.5)(n_{\downarrow} - 0.5), \quad (1)$$

the Wannier on-site energy for unoccupied sites should be reduced by  $0.5U$ , and the Wannier on-site energy for occupied sites should increase by  $0.5U$ . In our case, Co Wannier functions/sites are unoccupied; therefore, their on-site energy should be reduced by  $0.5U$ .

The starting point of CPT is disconnected clusters with a finite number of sites tiling the entire crystal lattice. The many-body Hamiltonian of these isolated clusters can be solved exactly, either by exact diagonalization or other appropriate methods, e.g., Monte Carlo simulation. In the next step, the neglected parts of the full Hamiltonian, i.e., the hopping terms between clusters, are treated perturbatively. This perturbative part can be accounted for exactly to all orders. Assuming that the Green's function of the system of disconnected clusters is  $G_0(\omega)$ , which is an infinite matrix in the site representation, the CPT Green's function is:

$$G(\omega) = [G_0(\omega)^{-1} - V]^{-1}, \quad (2)$$

where  $V$  is the part of the full Hamiltonian treated perturbatively. The problem of the infinite matrices is resolved using a Fourier transformation since all clusters form a periodic lattice themselves. One should note that even though both steps are exact, the final CPT Green's function is approximate; some many-body contributions are not fully accounted for. Nevertheless, this method represents a significant improvement in treating many-body correlations.

In our CPT model, the clusters are built from three interstitial Ta-character Wannier functions and one Co-centered Wannier function per spin. The  $\text{Co}_{1/3}\text{TaS}_2$  unit cell contains two clusters, as shown in Fig. 2(a). The Green's functions are calculated for real frequencies and at finite temperatures (300 K) using the Lehmann representation. The chemical potential is chosen to fix the average number of particles in the cluster and in the system. The calculated Green's function has wave-number periodicity corresponding to the  $\text{Co}_{1/3}\text{TaS}_2$  unit cell, i.e., the small Brillouin zone indicated by the red line in Fig. 2(c). The Green's function in the extended Brillouin zone (band unfolding) is obtained using Senechal's G-scheme (Green's function periodization) within CPT [51].

The results of the CPT calculations, expressed as the spectral function  $A(\vec{k}, \omega) = -\frac{1}{\pi} \text{Im} G(\vec{k}, \omega)$ , are presented and compared to the experimental band structure and the Fermi surface collected with  $h\nu = 72$  eV at 20 K in Fig. 2(b) and (c). Keeping in mind the simplicity of our model and the fact that ARPES intensities are further modulated by matrix element effects and finite experimental resolution we can see notable resemblance between experimental and calculated spectra.

The most prominent difference from the standard DFT+U results (presented in Fig. 6) is the emergence of a shallow electron-like band with its minimum located at the  $\bar{K}$  point,

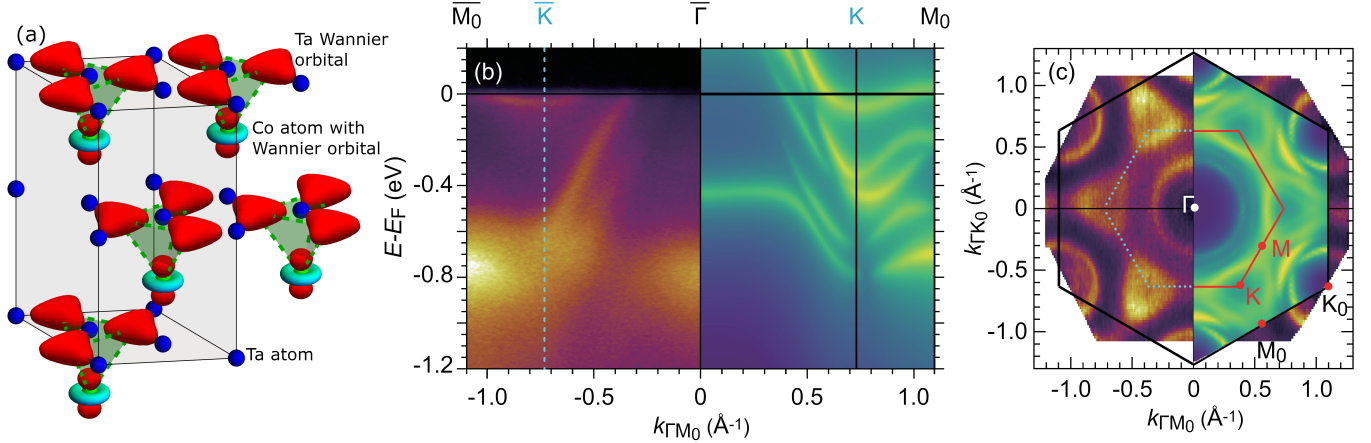


FIG. 2. (Color online) (a) Graphic representation of the crystal structure. Co atoms are shown as green spheres, overlaid with the corresponding Co Wannier orbitals. Red isosurfaces represent the interstitial Ta Wannier orbital lobes located between neighboring Ta atoms rather than at the atomic positions themselves (shown as blue spheres). Intra-cluster connections are indicated by dashed green lines and the clusters are shaded in green. The unit cell is indicated by a thin black line and shaded in gray. Sulfur atoms coordinating Ta in trigonal prismatic arrangement are omitted for clarity. These sulfur atoms occupy positions such that the edges of the trigonal prisms, connecting sulfur atoms in the layers above and below, do not intersect the Ta Wannier orbitals; that is, the sulfur triangles are rotated by  $30^\circ$  with respect to the triangles defined by the Wannier orbital positions. Comparisons of the spectra presented in Fig. 1 with the results of the CPT calculation: (b) the band structure along  $\bar{\Gamma}M_0$  direction and (c) the Fermi surface map of  $\text{Co}_{1/3}\text{TaS}_2$ .

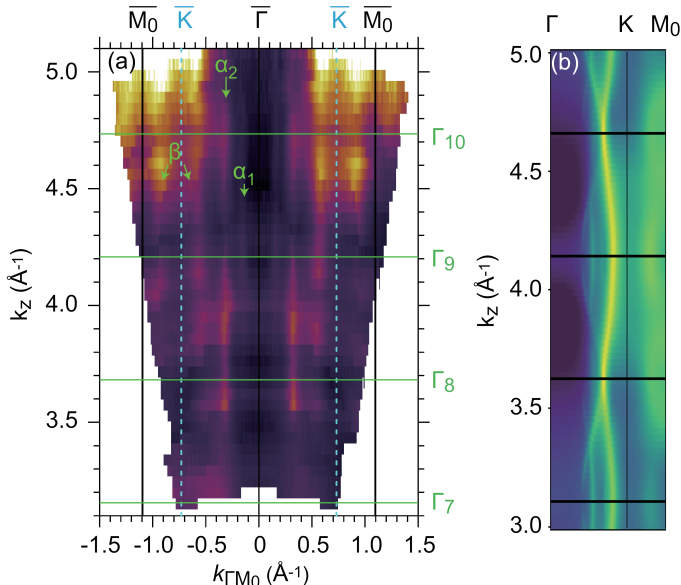


FIG. 3. (Color online) (a) ARPES intensity plot along the  $k_z$  direction at the Fermi level. The vertical dashed lines correspond to the boundaries of the  $\text{Co}_{1/3}\text{TaS}_2$  Brillouin zone. The horizontal green lines and labels ( $\Gamma_{n+1}$ ) mark the  $k_z$  levels corresponding to  $\Gamma_{n+1} \equiv (0, 0, 2\pi/c \times n)$ . (b) The CPT calculated Fermi surface along  $k_z$ -direction.

clearly visible on the right side in Fig. 2(b). In the corresponding Fermi surface map (Fig. 2(c)), this band forms a triangular contour around the  $\bar{K}$  point, closely reproducing the experimentally observed  $\beta$ -feature. The orbital character analysis indicates that this state has a substantial Co contribution. Its appearance only within the CPT framework, which treats

the Hubbard  $U$  beyond the mean-field level, provides strong evidence that the  $\beta$ -feature originates from strong electronic correlations, in line with our earlier conjecture. In contrast, the remaining bands in the CPT calculation are very similar to those from DFT+U, which already provides a satisfactory description of the corresponding experimental spectra. An exception is the spectral weight around 0.8 eV binding energy, which originates from the highest S-derived band (see Appendix B) and is not captured by our reduced CPT model.

It is important to stress that the present calculation is intentionally minimalistic, retaining only a limited set of bands near the Fermi level. Consequently, the residual discrepancies between CPT and experiment may arise from several sources: (i) the intrinsic approximations of the CPT method, (ii) the reduced orbital and spin manifold employed in the model, which effectively describes the Co sites by a single spin-1/2 orbital, whereas the real Co ions are in a high-spin  $S = 3/2$  configuration that requires the explicit inclusion of additional Co  $d$  orbitals and a proper treatment of Hund's rule coupling, (iii) the simplified treatment of the double-counting correction, and (iv) the neglect of direct hopping between intercalated Co atoms with opposite spin polarization. Additional factors, such as finite experimental resolution and the artificial broadening applied to the calculated spectra, are also expected to contribute.

Fig. 3 (a) shows the Fermi surface map of  $\text{Co}_{1/3}\text{TaS}_2$  along the  $k_z$  direction, obtained by varying photon energy from 30 to 90 eV in a few-eV steps. The data were processed using the same procedure as described in Refs. [10, 23]. The  $k_z$  dispersion plot reveals a two-dimensional (2D-like) Fermi surface,  $\alpha_2$ , visible at  $k_x \approx \pm 0.3 \text{\AA}^{-1}$ , which does not disperse with  $k_z$  and shows only variations in intensity. A faint additional 2D-like Fermi surface,  $\alpha_1$ , can also be observed near

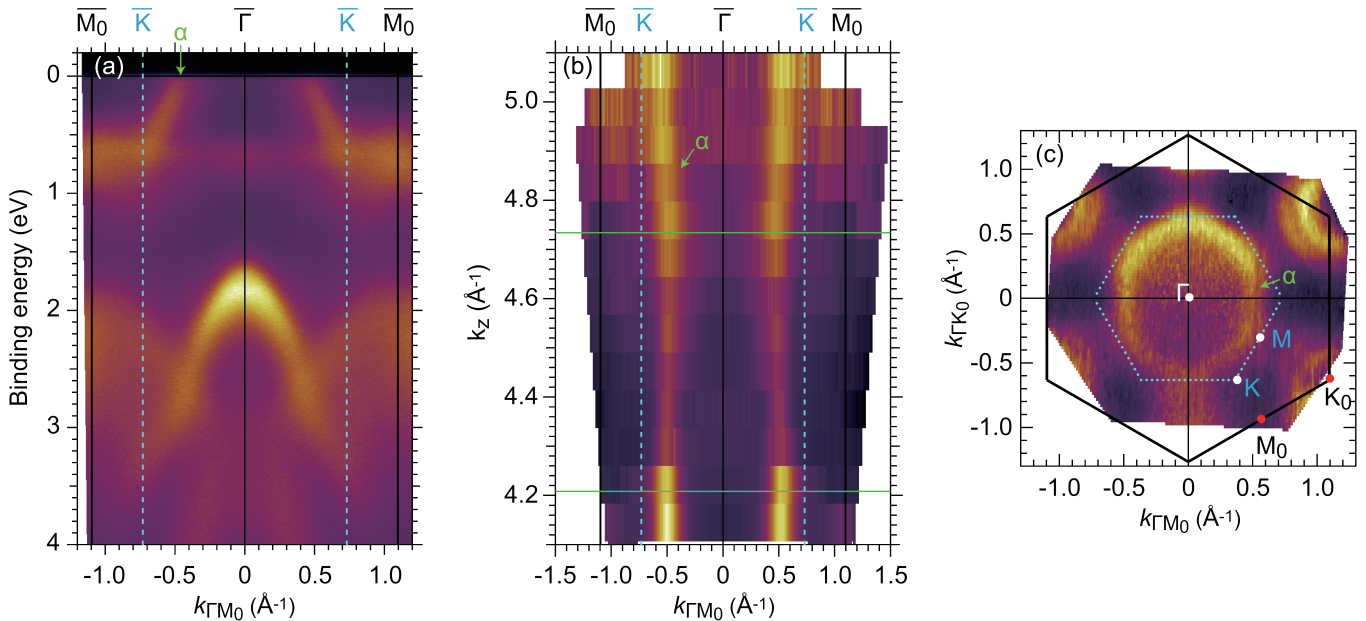


FIG. 4. (Color online) (a) ARPES intensity plot of  $\text{Co}_{0.22}\text{TaS}_2$  measured with  $h\nu=72$  eV at 20 K. (b) The Fermi surface along  $k_z$  direction obtained by changing photon energy from 57 to 90 eV with a step of 3 eV at 20 K. (c) The Fermi surface measured with  $h\nu=63$  eV at 20 K.

$k_x \approx \pm 0.15 \text{\AA}^{-1}$ , although it is too weak to be traced across all  $k_z$  values. Both features arise from the Ta  $d$  bands of 2H-TaS<sub>2</sub>: the outer band ( $\alpha_2$ ) corresponds to the antibonding state, while the inner ( $\alpha_1$ ), weaker one corresponds to the bonding state. DFT modeling predicts that the bonding band should exhibit noticeable  $k_z$  dispersion and cross the Fermi level between the  $\Gamma$  and  $\Lambda$  points. This likely explains why the  $\alpha_1$  band is not observed across all  $k_z$  values. In Fig. 3(a), it is only visible when it lies above the Fermi level which corresponds to  $\Lambda$  point. Indeed, the ARPES intensity plots measured with photon energies between  $h\nu = 38\text{--}50$  eV (see Fig. 6) show the bonding band ( $\alpha_1$ ) below the Fermi level. This photon energy range corresponds to  $k_z$  values below  $4 \text{\AA}^{-1}$  in Fig. 3(a), which accounts for the disappearance of the  $\alpha_1$  for low  $k_z$  values. This  $k_z$  dispersion agrees with the previously observed enhancement of  $c$ -axis electronic transport in TMDs upon Co intercalation, as discussed for  $\text{Co}_{1/3}\text{NbS}_2$  in Refs. [10, 36]. The  $\beta$ -feature appears in Fig. 3(a) at both sides of the  $\bar{K}$  point, with its intensity increasing at higher photon energies, consistent with the behavior seen in  $\text{Co}_{1/3}\text{NbS}_2$ .

Fig. 3(b) shows the same Fermi surface as in panel (a), but calculated using the CPT method. The  $\beta$ -feature is again visible on both sides of the  $K$  point. Ta  $d$  bands are also visible with antibonding band showing virtually no dispersion while bonding band exhibits strong  $k_z$  dependence. We also notice the characteristic periodicity of two Brillouin zones resulting from the fact that there are two Co and two Ta layers per one unit cell. The similar effect was already reported by Weber *et al.* [52] in  $\text{NbSe}_2$ .

Notably, we observed that the amount of Co intercalation strongly influences the presence of the  $\beta$ -feature. Fig. 4(a) shows the ARPES intensity plot of  $\text{Co}_{0.22}\text{TaS}_2$ . The measured band structure and Fermi surface resemble almost a rigid-

band-shifted 2H-TaS<sub>2</sub> band structure without the  $\beta$ -feature. By changing incident photon energy from 57 to 90 eV, in Fig. 4(b) we reconstructed the Fermi surface map along the  $k_z$ -direction. It shows a quasi-2D character with a small modulation, though no  $\beta$ -feature was observed within the experimental photon energy range. The central Fermi surface  $\alpha$ , around the  $\Gamma$  point, is observed at  $k_x \sim 0.5 \text{\AA}^{-1}$  very close to the one in 2H-TaS<sub>2</sub> [32] indicating a much smaller band shift compared to the 33% intercalated compound and suggesting even lower charge transfer. The same indication comes from the magnetic moment of  $\text{Co}_{1/3}\text{TaS}_2$  compared to  $\text{Co}_{0.22}\text{TaS}_2$ .  $\text{Co}_{1/3}\text{TaS}_2$  exhibits an effective magnetic moment of  $\sim 3.3 \mu_B$  similar to  $\text{Co}_{1/3}\text{NbS}_2$  [36]. Despite being reduced compared to the spin-only value  $\mu_{\text{eff}} = 3.87 \mu_B$  for  $S = 3/2$ , this moment is fully consistent with a  $\text{Co}^{2+}$  configuration once hybridization with the conduction band is taken into account, as demonstrated by DFT calculations [23, 36]. The underdoped compound  $\text{Co}_{0.22}\text{TaS}_2$  exhibits an effective magnetic moment of  $\sim 2.6 \mu_B$  obtained from the Curie-Weiss fit, close to the spin-only value  $2.83 \mu_B$  for  $S = 1$ , indicating a reduced effective spin state, consistent with a lower charge transfer. The lower charge transfer in underdoped compound implies that the lowest unoccupied Co orbital taken into account in our CPT is now below Fermi level, leaving only two remaining Co  $d$  orbitals above the Fermi level. This influences the energy spectrum, making it more similar to the Ni intercalated case where  $\beta$ -feature was much weaker and shallower [23]. Furthermore, the disorder inevitably present in  $\text{Co}_{0.22}\text{TaS}_2$ , as evidenced by the negative temperature dependence of the electrical resistivity and relatively broad ferromagnetic onset, predominantly affects the Co-derived electronic states, suppressing the coherence required for the formation of a well-defined  $\beta$ -feature. The remaining bands are TaS<sub>2</sub>-derived and

are much less affected by disorder, retaining sufficient coherence to remain observable in ARPES, although they appear significantly broadened. A difference is also seen in the shape of the central Fermi surface presented in Fig. 4(c), which in  $\text{Co}_{0.22}\text{TaS}_2$  exhibits a hexagonal form, similar to that observed in  $\text{Ni}_{1/3}\text{NbS}_2$  [23], in contrast to the circular Fermi surfaces of 33% Co intercalates [10, 11].

#### IV. CONCLUSION

We have investigated the electronic structure and Fermi surface of  $\text{Co}_{1/3}\text{TaS}_2$  and underdoped  $\text{Co}_{0.22}\text{TaS}_2$  using ARPES combined with advanced theoretical modeling of electronic correlations. Both compounds exhibit strong similarities to the parent 2H-TaS<sub>2</sub>, however, in the 33% intercalated compound a shallow electron pocket, the so-called  $\beta$ -feature, emerges as a clear deviation from a rigid-band shift. Unlike previous interpretations that ascribed this feature to the surface effects, cluster perturbation theory (CPT) modeling reproduces the  $\beta$ -feature and demonstrates that it originates from strong electronic correlations and is strongly influenced by the intercalated cobalt orbitals.

These results build on our earlier indications in  $\text{Co}_{1/3}\text{NbS}_2$ , where tight-binding modeling of DFT results combined with a slave boson approach suggested a correlation driven origin of the  $\beta$ -feature. Independently, DMFT calculations reported in the literature [37] pointed in a similar direction. In the present study, by employing CPT, we provide the first quantitative modeling that reproduces the experimental ARPES spectra of  $\text{Co}_{1/3}\text{TaS}_2$ , thereby directly demonstrating that strong electronic correlations are essential for understanding the low energy electronic structure of intercalated transition-metal dichalcogenides.

Furthermore, ARPES measurements on underdoped  $\text{Co}_{0.22}\text{TaS}_2$  reveal that the  $\beta$ -feature depends sensitively on electron doping, the orbital character of intercalant, and intrinsic disorder associated with the intercalated Co atoms. Our findings underscore the necessity of incorporating strong correlation effects in future theoretical studies of intercalated transition metal dichalcogenides.

#### ACKNOWLEDGEMENTS

We acknowledge insightful discussions with Eduard Tušić. This work has been partly supported by the Croatian Science Foundation under the project numbers IP-2020-02-9666, UIP-2019-04-2154 and IP-2022-10-3382, by the project: Ground states in competition - strong correlations, frustration and disorder - FrustKor financed by the Croatian Government and the European Union through the National Recovery and Resilience Plan 2021-2026 (NPOO) and by the project Cryogenic Centre at the Institute of Physics - KaCIF co-financed by the Croatian Government and the European Union through the European Regional Development Fund-Competitiveness and Cohesion Operational Programme

(Grant No. KK.01.1.1.02.0012). The research has been performed at the Elettra at the APE-LE beamline (proposal No. 20235254). NB acknowledges support by the project CeNIKS co-financed by the Croatian Government and the European Union through the European Regional Development Fund Competitiveness and Cohesion Operational Program (Grant No. KK.01.1.1.02.0013). The work at TU Wien was supported by the Austrian Science Fund (FWF) [10.55776/F86; 10.55776/P35945].

#### APPENDIX A. WANNIER FUNCTIONS AND HAMILTONIAN

The idea of using Wannier functions is to develop a Hubbard like model in which the Hubbard interaction on the intercalated atoms will be treated more accurately compared to DFT calculations. The Wannier functions can be extracted from DFT by using software package Wannier90 [41]. We have done two versions of Wannier calculations. The first one, that is focused on the energy range from  $E_F$ -7.7 eV to

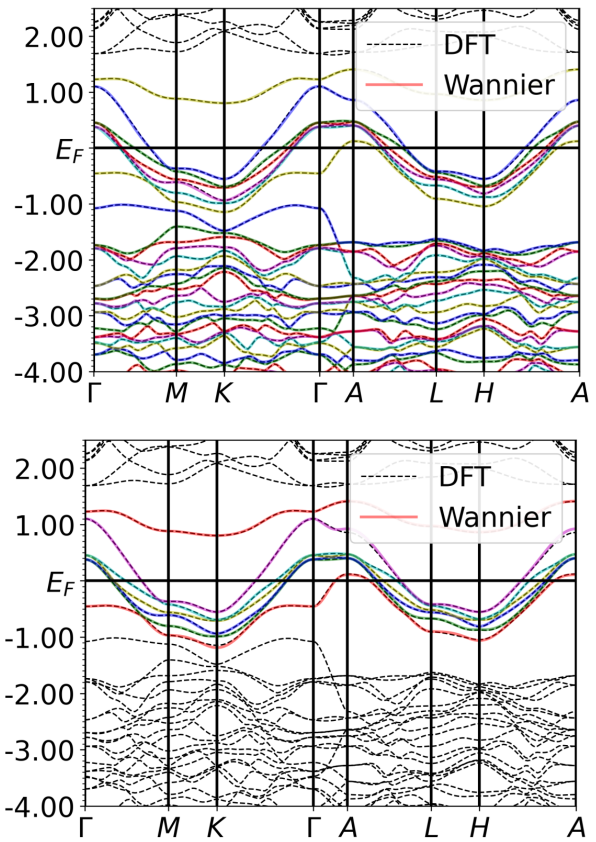


FIG. 5. Comparison of the DFT band structure (dotted lines) with the band structures obtained from the Wannier Hamiltonians, (solid lines). The upper panel shows the band structure constructed using 52 Wannier functions per unit cell, while the lower panel displays the result obtained with a reduced basis of 7 Wannier functions per unit cell.

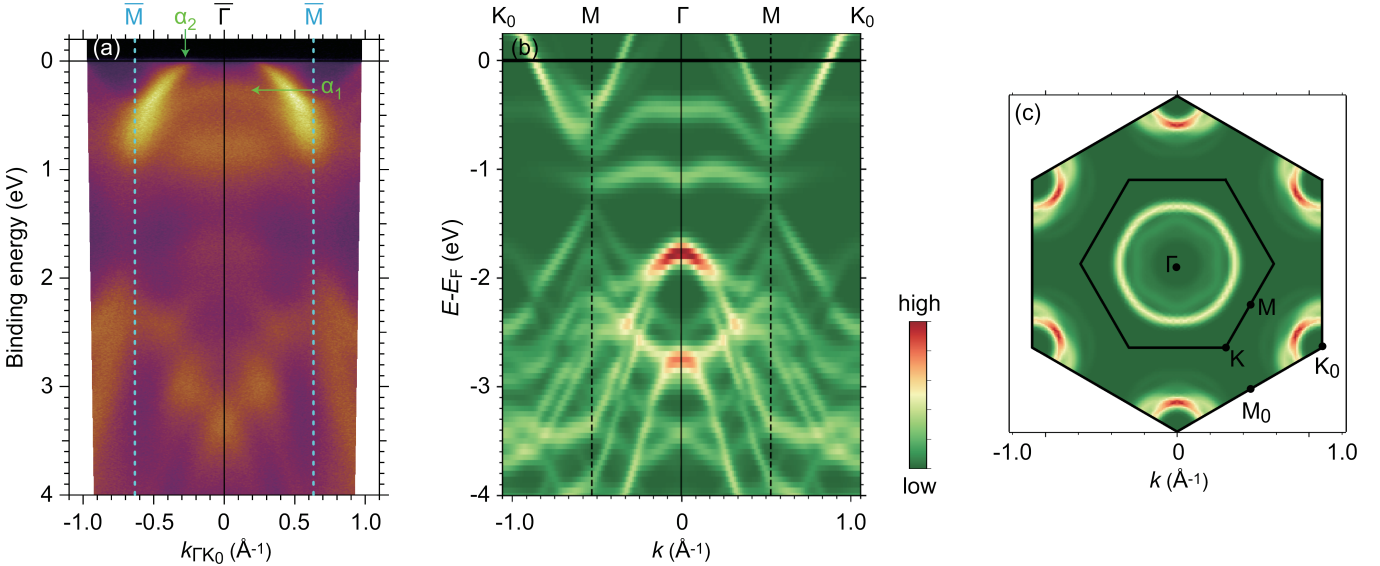


FIG. 6. (Color online) (a) ARPES spectra measured with  $h\nu=46$  eV photon energy along the high-symmetry  $\Gamma MK_0$  direction on  $\text{Co}_{1/3}\text{TaS}_2$ . (b) DFT calculated band structure of  $\text{Co}_{1/3}\text{TaS}_2$  unfolded into the first 2H-NbS<sub>2</sub> Brillouin zone using unfold-x package[53, 54]. (c) Fermi surface obtained by unfolding DFT calculated band structure. Inner hexagon represents the BZ of  $\text{Co}_{1/3}\text{TaS}_2$ , while the outer one represents the BZ of 2H-NbS<sub>2</sub>.

$E_F+1.5$  eV, is based on 52 Wannier function within the unit cell of  $\text{CoTa}_3\text{S}_6$ . The space localized nature of Wannier functions makes possible to create a tight-binding like Hamiltonian which can accurately reproduce DFT band structure within given energy range. The result is shown in Fig. 5 in the upper panel.

The second, simplified version of the Wannier calculation, is developed to describe the energy range just around the Fermi level, from  $E_F-1.0$  eV to  $E_F+1.5$  eV as this is the energy range where  $\beta$ -feature is observed. It is based on 7 Wannier functions in the unit cell. One may see that corresponding Hamiltonian can accurately reproduce 7 DFT bands around Fermi level, (the lower panel of Fig. 5). The top most Wannier band that is colored with red and is entirely above the Fermi level, has the largest contribution from lowest in energy empty Co *d*-state. The center of this Wannier function is located on Co atom. This Wannier function can be identified as an empty upper Hubbard state while the lower Hubbard state, that is occupied with an electron, is much lower in energy (around 6 eV) and it is outside the energy range in consideration. If this is a dispersion from spin up electrons, the center of Wannier function is located on the spin down Co ion, and *vice versa*. The centers of these Wannier functions depend on the electron spin in consideration. In spite of this differences between different spins, the band spectra for both spin projections are alike. The remaining 6 lower in energy bands have the largest contribution from Ta *d*-states. These Ta Wannier functions are not located on the Ta atoms, but in the points between three Ta atoms, in the space points not surrounded with sulphur atoms from above and below. These Wannier functions are shared with three neighboring Ta atoms. Their positions are inde-

pendent on the spin projection. The most prominent terms of the simplified Wannier Hamiltonian are listed in Table I. The largest hopping term in the Wannier Hamiltonian is between Co Wannier and Ta Wannier functions.

parameters	(eV)
$t(\text{Co-Ta})$	0.263293
$t(\text{Ta-Ta})$	0.064378
$t^{(2m)}(\text{Ta-Ta})$	0.132622
$t(\text{Co-Co})$	0.012778
$e(\text{Co})$	12.318694
$e(\text{Ta})$	11.412116

TABLE I. Dominant terms in the Wannier Hamiltonian.  $t$  are the first nearest neighbor hopping between Wannier orbitals,  $t^{(2m)}$  is the second nearest neighbor hopping and  $e$  are Wannier orbital's on-site energies. The double counting term is not subtracted.

## APPENDIX B. DFT+U UNFOLDING

In Fig. 6(a), the experimental ARPES spectra obtained along the high-symmetry  $\Gamma MK_0$  measured with  $h\nu=46$  eV are shown. In contrast to Fig. 1(a), where Ta bonding band is crossing the Fermi level forming the smallest, faint circular Fermi surface around  $\Gamma$  point in Fig. 1(b), here this band can be seen below Fermi level at the  $\Gamma$  point, together with the highest-lying S-derived band beneath it. In Fig. 6(b), DFT calculated band structure unfolded into the first Brillouin zone of 2H-NbS<sub>2</sub> is shown along the same high symmetry direction. In panel (c), the Fermi surface is shown. The most striking difference between Fig. 1(b) and Fig. 6(c) is the absence of  $\beta$ -feature in DFT calculated Fermi surface.

[1] F. Zhang, X. Miao, N. van Dijk, E. Brück, and Y. Ren, Advanced magnetocaloric materials for energy conversion: Recent progress, opportunities, and perspective, *Advanced Energy Materials* **14**, 2400369 (2024).

[2] R. H. Friend, A. R. Beal, and A. D. Yoffe, Electrical and magnetic properties of some first row transition metal intercalates of niobium disulphide, *The Philosophical Magazine: A Journal of Theoretical Experimental and Applied Physics* **35**, 1269 (1977).

[3] Z. Wang, R. Li, C. Su, and K. P. Loh, Intercalated phases of transition metal dichalcogenides, *SmartMat* **1**, e1013 (2020).

[4] P. Witte, A. M. van Koten, and M. E. Kamminga, Tuning the magnetic properties of van der Waals materials by intercalation, *Mater. Adv.*, 6702 (2024).

[5] T. Hatanaka, T. Nomoto, and R. Arita, Magnetic interactions in intercalated transition metal dichalcogenides: A study based on *ab initio* model construction, *Phys. Rev. B* **107**, 184429 (2023).

[6] L. Gao, M. Li, Q. Fan, K. Liang, B. Hu, and Q. Huang, Intercalation of metal into transition metal dichalcogenides in molten salts, *Small* **20**, 2304281 (2024).

[7] N. J. Ghimire, A. S. Botana, J. S. Jiang, J. Zhang, Y.-S. Chen, and J. F. Mitchell, Large anomalous Hall effect in the chiral-lattice antiferromagnet  $\text{CoNb}_3\text{S}_6$ , *Nature Communications* **9**, 3280 (2018).

[8] G. Tenasini, E. Martino, N. Ubrig, N. J. Ghimire, H. Berger, O. Zaharko, F. Wu, J. F. Mitchell, I. Martin, L. Forró, and A. F. Morpurgo, Giant anomalous Hall effect in quasi-two-dimensional layered antiferromagnet  $\text{Co}_{1/3}\text{NbS}_2$ , *Phys. Rev. Res.* **2**, 023051 (2020).

[9] S. Mangelsen, P. Zimmer, C. Näther, S. Mankovsky, S. Polesya, H. Ebert, and W. Bensch, Interplay of sample composition and anomalous Hall effect in  $\text{Co}_x\text{NbS}_2$ , *Phys. Rev. B* **103**, 184408 (2021).

[10] P. Popčević, Y. Utsumi, I. Bialo, W. Tabiš, M. A. Gala, M. Rosmus, J. J. Kołodziej, N. Tomaszewska, M. Garb, H. Berger, I. Batistić, N. Barišić, L. Forró, and E. Tutiš, Role of intercalated cobalt in the electronic structure of  $\text{Co}_{1/3}\text{NbS}_2$ , *Phys. Rev. B* **105**, 155114 (2022).

[11] H. Tanaka, S. Okazaki, K. Kuroda, R. Noguchi, Y. Arai, S. Minami, S. Ideta, K. Tanaka, D. Lu, M. Hashimoto, V. Kandyba, M. Cattelan, A. Barinov, T. Muro, T. Sasagawa, and T. Kondo, Large anomalous Hall effect induced by weak ferromagnetism in the noncentrosymmetric antiferromagnet  $\text{CoNb}_3\text{S}_6$ , *Phys. Rev. B* **105**, L121102 (2022).

[12] X. P. Yang, H. LaBollita, Z.-J. Cheng, H. Bhandari, T. A. Cochran, J.-X. Yin, M. S. Hossain, I. Belopolski, Q. Zhang, Y. Jiang, N. Shumiya, D. Multer, M. Liskevich, D. A. Usanov, Y. Dang, V. N. Strocov, A. V. Davydov, N. J. Ghimire, A. S. Botana, and M. Z. Hasan, Visualizing the out-of-plane electronic dispersions in an intercalated transition metal dichalcogenide, *Phys. Rev. B* **105**, L121107 (2022).

[13] Y. Liu, Z. Hu, X. Tong, E. D. Bauer, and C. Petrovic, Electrical and thermal transport in van der Waals magnets  $2H\text{-M}_x\text{TaS}_2$  ( $\text{M} = \text{Mn, Co}$ ), *Phys. Rev. Res.* **4**, 013048 (2022).

[14] P. Park, Y.-G. Kang, J. Kim, K. H. Lee, H.-J. Noh, M. J. Han, and J.-G. Park, Field-tunable toroidal moment and anomalous hall effect in noncollinear antiferromagnetic weyl semimetal  $\text{Co}_{1/3}\text{TaS}_2$ , *npj Quantum Materials* **7**, 42 (2022).

[15] H. Takagi, R. Takagi, S. Minami, T. Nomoto, K. Ohishi, M.-T. Suzuki, Y. Yanagi, M. Hirayama, N. D. Khanh, K. Karube, H. Saito, D. Hashizume, R. Kiyanagi, Y. Tokura, R. Arita, T. Nakajima, and S. Seki, Spontaneous topological Hall effect induced by non-coplanar antiferromagnetic order in intercalated van der Waals materials, *Nature Physics* **19**, 961 (2023).

[16] J. van den Berg and P. Cossee, Structural aspects and magnetic behaviour of  $\text{NbS}_2$  and  $\text{TaS}_2$  containing extra metal atoms of the first transition series, *Inorganica Chimica Acta* **2**, 143 (1968).

[17] S. S. P. Parkin and R. H. Friend, 3d transition-metal intercalates of the niobium and tantalum dichalcogenides. I. Magnetic properties, *Philosophical Magazine B* **41**, 65 (1980).

[18] S. S. P. Parkin and R. H. Friend, 3d transition-metal intercalates of the niobium and tantalum dichalcogenides. II. Transport properties, *Philosophical Magazine B* **41**, 95 (1980).

[19] S. S. P. Parkin, E. A. Marseglia, and P. J. Brown, Magnetic structure of  $\text{Co}_{1/3}\text{NbS}_2$  and  $\text{Co}_{1/3}\text{TaS}_2$ , *Journal of Physics C: Solid State Physics* **16**, 2765 (1983).

[20] P. Park, W. Cho, C. Kim, Y. An, M. Avdeev, K. Iida, R. Kajimoto, and J.-G. Park, Composition dependence of bulk properties in the Co-intercalated transition metal dichalcogenide  $\text{Co}_{1/3}\text{TaS}_2$ , *Phys. Rev. B* **109**, L060403 (2024).

[21] P. Park, W. Cho, C. Kim, Y. An, Y.-G. Kang, M. Avdeev, R. Sibille, K. Iida, R. Kajimoto, K. H. Lee, W. Ju, E.-J. Cho, H.-J. Noh, M. J. Han, S.-S. Zhang, C. D. Batista, and J.-G. Park, Tetrahedral triple-Q magnetic ordering and large spontaneous Hall conductivity in the metallic triangular antiferromagnet  $\text{Co}_{1/3}\text{TaS}_2$ , *Nature Communications* **14**, 8346 (2023).

[22] N. Sirica, S.-K. Mo, F. Bondino, I. Pis, S. Nappini, P. Vilmercati, J. Yi, Z. Gai, P. C. Snijders, P. K. Das, I. Vobornik, N. Ghimire, M. R. Koehler, L. Li, D. Sapkota, D. S. Parker, D. G. Mandrus, and N. Mannella, Electronic structure of the chiral helimagnet and 3d-intercalated transition metal dichalcogenide  $\text{Cr}_{1/3}\text{NbS}_2$ , *Physical Review B* **94**, 075141 (2016).

[23] Y. U. Boucher, I. Bialo, M. A. Gala, W. Tabiš, M. Rosmus, N. Olszowska, J. J. Kołodziej, B. Gudac, M. Novak, N. K. C. Muniraju, I. Batistić, N. Barišić, P. Popčević, and E. Tutiš, Intercalation-induced states at the fermi level and the coupling of intercalated magnetic ions to conducting layers in  $\text{Ni}_{1/3}\text{NbS}_2$ , *Phys. Rev. B* **109**, 085135 (2024).

[24] G. Panaccione, I. Vobornik, J. Fujii, D. Krizmancic, E. Anane, L. Giovanelli, F. Maccherozzi, F. Salvador, A. De Luisa, D. Benedetti, A. Gruden, P. Bertoč, F. Polack, D. Cocco, G. Sostero, B. Diviacco, M. Hochstrasser, U. Maier, D. Pescia, C. H. Back, T. Greber, J. Osterwalder, M. Galaktionov, M. Sancrotti, and G. Rossi, Advanced photoelectric effect experiment beamline at elettra: A surface science laboratory coupled with synchrotron radiation, *Review of Scientific Instruments* **80**, 043105 (2009).

[25] P. Giannozzi, S. Baroni, N. Bonini, M. Calandra, R. Car, C. Cavazzoni, D. Ceresoli, G. L. Chiarotti, M. Cococcioni, I. Dabo, A. D. Corso, S. de Gironcoli, S. Fabris, G. Fratesi, R. Gebauer, U. Gerstmann, C. Gougaussis, A. Kokalj, M. Lazzeri, L. Martin-Samos, N. Marzari, F. Mauri, R. Mazzarello, S. Paolini, A. Pasquarello, L. Paulatto, C. Sbraccia, S. Scandolo, G. Sclauzero, A. P. Seitsonen, A. Smogunov, P. Umari, and R. M. Wentzcovitch, Quantum espresso: a modular and open-source software project for quantum simulations of materials, *Journal of Physics: Condensed Matter* **21**, 395502 (2009).

[26] P. Giannozzi, O. Andreussi, T. Brumme, O. Bunau, M. B. Nardelli, M. Calandra, R. Car, C. Cavazzoni, D. Ceresoli, M. Cococcioni, N. Colonna, I. Carnimeo, A. D. Corso, S. de Gironcoli, P. Delugas, R. A. DiStasio, A. Ferretti,

A. Floris, G. Fratesi, G. Fugallo, R. Gebauer, U. Gerstmann, F. Giustino, T. Gorni, J. Jia, M. Kawamura, H.-Y. Ko, A. Kokalj, E. Küçükbenli, M. Lazzeri, M. Marsili, N. Marzari, F. Mauri, N. L. Nguyen, H.-V. Nguyen, A. O. de-la Roza, L. Paulatto, S. Poncé, D. Rocca, R. Sabatini, B. Santra, M. Schlipf, A. P. Seitsonen, A. Smogunov, I. Timrov, T. Thonhauser, P. Umari, N. Vast, X. Wu, and S. Baroni, Advanced capabilities for materials modelling with quantum espresso, *Journal of Physics: Condensed Matter* **29**, 465901 (2017).

[27] S. L. Dudarev, G. A. Botton, S. Y. Savrasov, C. J. Humphreys, and A. P. Sutton, Electron-energy-loss spectra and the structural stability of nickel oxide: An LSDA+U study, *Phys. Rev. B* **57**, 1505 (1998).

[28] I. Timrov, N. Marzari, and M. Cococcioni, Hubbard parameters from density-functional perturbation theory, *Phys. Rev. B* **98**, 085127 (2018).

[29] I. Timrov, N. Marzari, and M. Cococcioni, Self-consistent Hubbard parameters from density-functional perturbation theory in the ultrasoft and projector-augmented wave formulations, *Phys. Rev. B* **103**, 045141 (2021).

[30] I. Timrov, N. Marzari, and M. Cococcioni, HP – A code for the calculation of Hubbard parameters using density-functional perturbation theory, *Computer Physics Communications* **279**, 108455 (2022).

[31] N. Marzari, D. Vanderbilt, A. De Vita, and M. C. Payne, Thermal contraction and disordering of the Al(110) surface, *Phys. Rev. Lett.* **82**, 3296 (1999).

[32] L. Camerano, D. Mistrulli, D. Pierucci, J. Dai, M. Tallarida, L. Ottaviano, G. Profeta, and F. Bisti, Darkness in interlayer and charge density wave states of 2H-TaS<sub>2</sub>, *Phys. Rev. B* **111**, L121112 (2025).

[33] J. Zhao, K. Wijayaratne, A. Butler, J. Yang, C. D. Malliakas, D. Y. Chung, D. Louca, M. G. Kanatzidis, J. van Wezel, and U. Chatterjee, Orbital selectivity causing anisotropy and particle-hole asymmetry in the charge density wave gap of 2H-TaS<sub>2</sub>, *Phys. Rev. B* **96**, 125103 (2017).

[34] K. Wijayaratne, J. Zhao, C. Malliakas, D. Young Chung, M. G. Kanatzidis, and U. Chatterjee, Spectroscopic signature of moment-dependent electron-phonon coupling in 2H-TaS<sub>2</sub>, *J. Mater. Chem. C* **5**, 11310 (2017).

[35] N. Sirica, P. Vilmercati, F. Bondino, I. Pis, S. Nappini, S. K. Mo, A. V. Fedorov, P. K. Das, I. Vobornik, J. Fujii, L. Li, D. Sapkota, D. S. Parker, D. G. Mandrus, and N. Mannella, The nature of ferromagnetism in the chiral helimagnet Cr<sub>1/3</sub>NbS<sub>2</sub>, *Communications Physics* **3**, 1 (2020).

[36] P. Popčević, I. Batistić, A. Smontara, K. Velebit, J. Jaćimović, I. Živković, N. Tsyrulin, J. Piatek, H. Berger, A. Sidorenko, H. Rønnow, L. Forró, N. Barišić, and E. Tutti, Electronic transport and magnetism in the alternating stack of metallic and highly frustrated magnetic layers in Co<sub>1/3</sub>NbS<sub>2</sub>, *Phys. Rev. B* **107**, 235149 (2023).

[37] H. Park and I. Martin, DFT + DMFT study of the magnetic susceptibility and the correlated electronic structure in transition-metal intercalated NbS<sub>2</sub>, *Phys. Rev. B* **109**, 085110 (2024).

[38] C. Gros and R. Valentí, Cluster expansion for the self-energy: A simple many-body method for interpreting the photoemission spectra of correlated fermi systems, *Phys. Rev. B* **48**, 418 (1993).

[39] D. Sénéchal, D. Perez, and M. Pioro-Ladrière, Spectral weight of the hubbard model through cluster perturbation theory, *Phys. Rev. Lett.* **84**, 522 (2000).

[40] D. Sénéchal, D. Perez, and D. Plouffe, Cluster perturbation theory for hubbard models, *Phys. Rev. B* **66**, 075129 (2002).

[41] G. Pizzi, V. Vitale, R. Arita, S. Blügel, F. Freimuth, G. Géranton, M. Gibertini, D. Gresch, C. Johnson, T. Koretsune, J. I. nez Azpiroz, H. Lee, J.-M. Lihm, D. Marchand, A. Mazzocco, Y. Mokrousov, J. I. Mustafa, Y. Nohara, Y. Nomura, L. Paulatto, S. Poncé, T. Ponweiser, J. Qiao, F. Thöle, S. S. Tsirkin, M. Wierzbowska, N. Marzari, D. Vanderbilt, I. Souza, A. A. Mostofi, and J. R. Yates, Wannier90 as a community code: new features and applications, *Journal of Physics: Condensed Matter* **32**, 165902 (2020).

[42] S. Ryee and M. J. Han, The effect of double counting, spin density, and hund interaction in the different DFT+U functionals, *Scientific Reports* **8**, 9559 (2018).

[43] S. Ryee and M. J. Han, Comparative study of DFT+U functionals for non-collinear magnetism, *Journal of Physics: Condensed Matter* **30**, 275802 (2018).

[44] M. Karolak, G. Ulm, T. Wehling, V. Mazurenko, A. Poteryaev, and A. Lichtenstein, Double counting in LDA+DMFT-The example of NiO, *Journal of Electron Spectroscopy and Related Phenomena* **181**, 11 (2010), proceedings of International Workshop on Strong Correlations and Angle-Resolved Photoemission Spectroscopy 2009.

[45] H. Park, A. J. Millis, and C. A. Marianetti, Computing total energies in complex materials using charge self-consistent DFT + DMFT, *Phys. Rev. B* **90**, 235103 (2014).

[46] I. A. Nekrasov, V. S. Pavlov, and M. V. Sadovskii, Consistent LDA' + DMFT—an unambiguous way to avoid double counting problem: NiO test, *JETP Letters* **95**, 581 (2012).

[47] G. Kotliar, S. Y. Savrasov, K. Haule, V. S. Oudovenko, O. Parcollet, and C. A. Marianetti, Electronic structure calculations with dynamical mean-field theory, *Rev. Mod. Phys.* **78**, 865 (2006).

[48] M. I. Katsnelson, V. Y. Irkhin, L. Chioncel, A. I. Lichtenstein, and R. A. de Groot, Half-metallic ferromagnets: From band structure to many-body effects, *Rev. Mod. Phys.* **80**, 315 (2008).

[49] K. Haule, Exact double counting in combining the dynamical mean field theory and the density functional theory, *Phys. Rev. Lett.* **115**, 196403 (2015).

[50] E. Plekhanov, P. Hasnip, V. Sacksteder, M. Probert, S. J. Clark, K. Refson, and C. Weber, Many-body renormalization of forces in *f*-electron materials, *Phys. Rev. B* **98**, 075129 (2018).

[51] D. Sénéchal, Cluster perturbation theory, in *Strongly Correlated Systems, Theoretical Methods*, edited by F. M. Adolfo Avella (Springer Berlin, Heidelberg, 2012) Chap. 8, pp. 237–270.

[52] F. Weber, R. Hott, R. Heid, L. L. Lev, M. Caputo, T. Schmitt, and V. N. Strocov, Three-dimensional Fermi surface of 2H-NbSe<sub>2</sub>: Implications for the mechanism of charge density waves, *Physical Review B* **97**, 235122 (2018).

[53] V. Popescu and A. Zunger, Extracting  $e$  versus  $\vec{k}$  effective band structure from supercell calculations on alloys and impurities, *Phys. Rev. B* **85**, 085201 (2012).

[54] D. Pacilè, C. Cardoso, G. Avvisati, I. Vobornik, C. Mariani, D. A. Leon, P. Bonfà, D. Varsano, A. Ferretti, and M. G. Betti, Narrowing of d bands of FeCo layers intercalated under graphene, *Applied Physics Letters* **118**, 121602 (2021).